Environment-controlled sol-gel soft-NIL processing for optimized titania, alumina, silica and yttria-zirconia imprinting at sub-micron dimensions

Thomas Bottein, Olivier Dalstein, Magali Putero, Andrea Cattoni, Marco Faustini, Marco Abbarchi, David Grosso

Environment-Controlled Sol-Gel Soft-NIL Processing for Optimized Titania, Alumina, Silica and Yttria-Zirconia Imprinting at Sub-Micron Dimensions.

Thomas Bottein[1], Olivier Dalstein[2], Magali Putero[1], Andrea Cattoni[3], Marco Faustini[2], Marco Abbarchi[1], David Grosso[1*]

Metal oxides (MO_X) surface nanopatterns can be prepared using Soft-Nano-Imprint-Lithography (soft-NIL) combined with sol-gel deposition processing. Even if sol-gel layers remain gel-like straight after deposition, their accurate replication from a mould remains difficult as a result of the fast evaporation-induced stiffening that prevents efficient mass transfer underneath the soft mould. The present work reports a detailed investigation of the role of the xerogel layer conditioning (temperature and relative humidity) prior to imprinting and its influence on the quality of the replication. The study is performed on four different systems namely Titania, Alumina, Silica and Yttria-stabilised Zirconia. We demonstrate that the quality of the replica can be considerably improved without the use of sacrificial stabilising organic agents, but by simply applying an optimal aging in controlled temperature and relative humidity specific to each different reported MO_X. In each case this condition corresponds to swelling the initial xerogels of around 30%$_{vol}$ by water absorption from humidity. We show that this degree of swelling represents the best compromise for sufficiently increase the xerogel fluidity while limiting the shrinkage upon final thermal curing.

Introduction.

Lithography techniques are nowadays essential to design structures at the nanoscale in numerous fields such as integrated circuits, organic electronics, photonics, lightning, or displays to name a few. Most reported lithography methods are based on microfabrication technology often involving processes such as chemical vapour deposition [1], laser ablation [2], e-beam lithography, reactive ion[3–5] or chemical etching[6], indirect nanoimprint lithography [7], interferential lithography [8], nanosphere lithography [9,10], and solid state dewetting [11,12]. These methods are generally cumbersome and involve many steps, making them difficult to scale-up to large surfaces. Amongst them, Soft-Nano Imprint Lithography (Soft-NIL) appears as the most appropriate for large surface processing as demonstrated on 6-inch silicon wafers for broad-band and wide-angle anti-reflection nano patterned coatings [7]. It also has the advantage of involving a limited number of simple steps often taking place in mild conditions (T_{amb}, P_{atm}), allowing for limited long-range deformation, high throughput and high resolution [13,14] on a plethora of different substrates. [15,16]

Most soft-NIL processes involve the use of a resist, often photocurable or thermoplastic polymers, as they can stiffen by cross-liking upon UV or high temperature exposure, respectively. This makes the faithful templating and the demoulding of such organic-based replica relatively easy. [14]

Applying soft-NIL approaches to process metal oxides is also very appealing as a result of the multiple functionalities that can be created with these ceramics in view of their broad and various chemical and physical intrinsic properties.[17] However, their direct imprinting is quasi-unachievable due to the impossibility to change the viscosity of the ceramic in moderate conditions.

An already promising soft-NIL method of MO_X exploits as-deposited sol-gel layers, also addressed as xerogel layers. These are poorly cross-linked flexible networks of sol-gel organometallic precursors or hydrolysed intermediates, that stiffen upon drying, poly-condensation, and finally thermal annealing, to form the final thermodynamically (meta-)stable oxides. These properties can be exploited in soft-NIL at two conditions: (i) that imprinting takes place when the layer is under a gel-like form and (ii) the demoulding is made after sufficient solidification. Both these controls are challenging in sol-gel since the as-deposited layers undergo more or less fast

[1] *NOVA Team, Institut Matériaux Microélectronique et Nanosciences de Provence, (IM2NP) - UMR CNRS 7334, Aix-Marseille Université, Faculté des Sciences de Saint Jérôme, 13397 Marseille Cedex 20, France.*
[2] *Sorbonne Universités, UPMC Univ Paris 06, CNRS, Collège de France, UMR 7574, Chimie de la Matière Condensée de Paris, F-75005, Paris, France.*
[3] *Laboratoire de Photonique et de Nanostructures (LPN) - CNRS, route de Nozay, 91460 Marcoussis, France.*
[*] *david.grosso@univ-amu.fr*
Electronic Supplementary Information (ESI) available: [details of any supplementary information available should be included here]. See DOI: 10.1039/x0xx00000x

cross-linking upon drying and mild thermal activation. These phenomena are generally accompanied by the release of water or solvent molecules that are trapped within the materials underneath the mould, affecting the replica morphology, density and shrinkage factor. For instance, TetraEthOxySilane (TEOS), a conventional silica precursor in sol-gel chemistry, can be used in Soft-NIL processes but it usually provides gel-like intermediates featuring a too rapid drying. Alternatively, MethylTrieEthOxySilane (MTEOS) is used to decrease the condensation rate of the silica network[18] due to the non-hydrolysable CH_3-Si bond. Eventually, the hybrid silica converts into a purely inorganic structure after calcination.[19–21] Non-silica metal oxides are also very interesting systems to pattern. However, only a few works addressing ZnO [22], ITO [23], PZT [24] or TiO_2 [15] were reported, all underlining the high potential but the great difficulties intrinsic to the involved chemistries.

In the case of these transition metal oxides, one relies on sol-gel approaches and on the use of polymeric or organic stabilizing agents in order to adjust the rheology and the precursor reactivity and achieve a good resolution and a large geometrical aspect ratio of the final 3D structures. However, the main drawback associated to this approach is the high shrinkage due to the elimination of organic moieties during the annealing step.[20,25–28] Very recently, it has been showed that the direct imprinting of sol gel formulations containing metal oxides nanoparticles (NPs) can reduce the shrinkage. [29] However, owing to their toxicity, their handling remains an issue for mass production. In addition, the obtained materials have low density (measured refractive index n=2 against 2.45 for dense TiO_2) resulting from the presence of pores associated with the packing of NPs. Recently, TiO_2 diffraction gratings for gas sensing transduction[15] and dielectric Mie resonator arrays for light trapping [16] were produced from $TiCl_4$ stabilising-agent-free sol-gel solutions, using a pressure-less Soft-NIL method relying on PDMS mould outgassing. On the one hand, these conditions already allowed for a reduced shrinkage factor. On the other hand, the viscosity of the intermediate xerogel is high, preventing efficient mass transfer within the sharp features of the mould. Both effects led to relatively low aspect ratio of the nano-imprinted structures limiting the potential applications of these MO_X-based patterns. Indeed, applications of these TiO_2 patterns in photonics[16,30–33] for example require extremely well-controlled morphologies and large enough aspect-ratio.

A solution to obtain MO_X replica exhibiting such optimised characteristics would require to use a minimal amount of fluidizing (stabilising) sacrificial agent into the xerogel for an efficient mass transfer, as well as a limited shrinkage after densification. Ideally, this agent may induce fluidization of the xerogel when incorporated in small volume fraction and may also be easily incorporated and removed from the xerogel when necessary along the imprinting process. All these criteria are met with water since (i) it is amongst the smallest molecules; (ii) its presence at the molecular level in the coordination and solvation spheres of the intermediate metallic complexes allows them to interact through weak flexible hydrogen bonds and prevents them to condense too rapidly by forming oxo or hydroxo bridges;[34] (iii) it can be easily absorbed or withdrawn from the hygroscopic xerogels through dynamic equilibrium with the environment, meaning that its volume proportion in the xerogel can be controlled by the environmental relative humidity; (iv) it can be easily eliminated through pumping into the vacuumed moulds. The use of atmospheric water to adjust the fluidity during imprinting was already exploited for PEDOT:PSS polymeric resists to improve the quality of the replica.[28] However, applying this additional control during processing of sol-gel systems, for which water is also a reactive for the condensation reaction, has never been reported to the best of our knowledge.

In the present work, we demonstrate that the quality of 3D structures of nano-imprinted conventional sol-gel systems such as Titania, Alumina, Silica and Yttria-stabilised Zirconia, can be considerably improved in terms of resolution, aspect ratio, and long-range homogeneity, by simply adjusting the humidity and temperature during the process without the use of additional organic agents.[35] We further show that the method is compatible with high throughput processes and provides excellent reproducibility as long as the proper temperature/relative humidity/aging time coupled values are applied for a specific xerogel. Interestingly, we show that for each system, optimal results are obtained when the volume fraction of weakly bound water in the xerogel is around 30%.

These results are accounted for by systematic investigations of the xerogel water uptake with respect to relative humidity and temperature via in situ environmental spectroscopic ellipsometry, and by monitoring the morphology and homogeneity of the final patterns through atomic force microscopy, electronic microscopy, and dark-field optical microscopy.

Experimental.

- Moulds were prepared from the following procedure: Si masters were elaborated with different features and periodicities using FIB (Focused Ion Beam) or EBL (Electron Beam Lithography coupled to reactive ion etching) on Si wafers. Their surfaces were first made hydrophobic by immersion for 10 min in a solution of 0.05M $SiCl_2(CH_3)_2$ in ethanol before being thoroughly rinsed with ethanol and acetone. PDMS (PolyDyMethylSiloxane) reactants (90w% RTV141A; 10w% RTV141B from BLUESIL) were poured onto the master and cured at 70°C for 1h before unmoulding. [36]

- Sol-gel initial solutions were prepared from TEOS (TetraEthylOrthoSilicate), MTEOS (MethylTriEtOxySilane), $TiCl_4$, $Zr(Cl)_4$, $Y(NO_3)_3,2H_2O$, $Al(OiPr)_3$, Pluronic F127 (Poyethylene oxide-Polypropylene oxide triblock copolymer) and CTAB (CetylTrimethylAmmonium Bromide), deionized water, absolute ethanol (EtOH), and concentrated hydrochloric acid (HCl). CTAB and F127 are added in very low molar fractions in the present work to enhance the wetting property of the sol. The added quantity is in no cases enough to play the role of micellar template for pore generation.[17] CTAB is usually

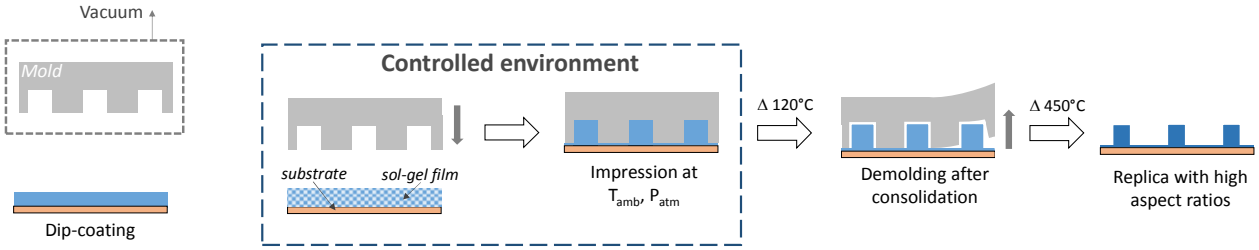

Figure 1: *Schematic representation of the successive steps involved in the soft-NIL/sol-gel processing. The controlled environment was performed using a computer-piloted set of mass flow controllers delivering air at a constant flow and temperature, and at humidity adjusted between 2 and 98% with 2% error. The xerogel layer/substrate sample stands on a heating plate (not-shown) in the chamber to increase slightly the temperature if required.*

preferred since it does not change much the xerogel viscosity. When CTAB interacts too much with the inorganic molecular precursors, such as with Ti(IV) and Zr(IV), its surface energy reducing effect is less efficient and Pluronic types amphiphilic agents can be used, in spite of the associated viscosity increase. [37,38] TiO_2 precursor solution is composed of 1 $TiCl_4$; 40 EtOH; 7 H_2O; 2.10^{-4} F127 molar ratios. Al_2O_3 precursor solution is composed of 1 $Al(OiPr)_3$; 29 EtOH; 4.8 H_2O; 1.4 HCl; 4.10^{-3} CTAB molar ratios. This solution was filtered with a 0.45 µm PTFE membrane before use. Yttria-stabilised zirconia precursor solution is composed of 0.94 $Zr(Cl)_4$; 0.06 $Y(NO_3)_3,2H_2O$; 41 EtOH; 12 H_2O; 2.10^{-4} F127 molar ratios. Silica was obtained from a solution containing 1 TEOS; 40 EtOH; 10 H_2O; 0.01 HCl; 0.01 CTAB molar ratios. For hybrid silica solution, 2/5 (in mole) of TEOS was replaced by MTEOS. Solutions were stirred 24 hours at room temperature prior to use.

- Xerogel films were prepared by dip-coating using an ACEdip equipment from SolGelWay. Depositions were made on glass or on Si (100) substrates at constant relative humidity of 20% and with controlled withdrawal speeds between 1 and 6 $mm.s^{-1}$ in order to adjust the final thickness. After dip-coating, the substrates were quickly introduced in a custom-designed chamber allowing accurate control of the atmosphere composition using mass-flow controllers sets (ACEflow from SolGelWay). A controlled flow of air or nitrogen with adjusted relative humidity, and/or relative vapour pressures in any volatile species, can be introduced into the chamber during manipulation. The temperature of the xerogel layer could be increased from 22°C to 28°C using a heating plate localized inside the chamber, while the atmosphere was maintained at 22°C using the constant humidity-controlled air flow.
- Imprinting of sol-gel films with PDMS mould involves the following steps illustrated in Figure 1. First, moulds were degassed under vacuum (10 mbar) for 20 min before direct application on the as-prepared xerogel films standing in controlled environment, without additional pressure. In these conditions, and because of the several-millimeters thick mould, the equilibrium with the atmosphere is slow enough to allow for the latter to keep its pumping efficiency over several tens of minutes. After 2 min, the samples were transferred in a 70°C stove for 1 min then in a 120°C stove for 1 min to consolidate the xerogel films before peeling off the PDMS mould. Finally, if not stated otherwise, the sol-gel replicas were annealed at 450°C for 10 min for consolidation.

Refractive index dispersion and thickness of the xerogels and non-patterned calcined films were characterized using a spectroscopic Ellipsometry (Woollam M2000V) system equipped with micro-focused probes. Refractive index of TiO_2 was measured to be $n(\lambda) = 2.05 + 0.05/\lambda^2$ after annealing at 450°C/10min (Cauchy model with λ in µm) with $k(\lambda) = 0$ in the visible range. Refractive index was found to be $n(\lambda) = 1.66 + 0.001/\lambda^2$ for Al_2O_3 (1000°C/2h), $n(\lambda) = 1.85 + 0.012/\lambda^2$ for Y-ZrO_2 (450°C/10min) and $n(\lambda) = 1.43 + 0.003/\lambda^2$ for silica (450°C/10min). Environmental modulation of the xerogel characteristics was followed by time-resolved ellipsometry while the atmosphere composition and temperature were controlled in the ellipsometry chamber using a mass-flow controller system (ACEFlow device from SolGelWay) and a heating device (Linkam T96-HT). Structural investigation of the nano-imprinted samples was performed by Atomic Force Microscopy (AFM) (PSIA XE-100 AFM) and high-resolution scanning electron microscopy (Dual-beam FIB HELIOS 600 nanolab & SEM-FEG Magellan 400L FEI). Optical microscope Dark Field images were performed with a commercial LEICA DMI5000M microscope with a 100x objective lens (N.A. = 0.75). X-ray Diffraction (XRD) patterns were recorded on a conventional diffractometer in Bragg–Brentano geometry (PANalytical Empyrean) using Cu radiation (λ = 0.154 nm), a rapid detector (PANalytical PIXcel) and an offset of 1.5 degrees in order to avoid Si substrate contribution. Grazing incidence XRD (GIXRD) analyses were performed on the same set-up with a parallel plate collimator 0.27 degrees at various incident angles (ω from 1 to 3 degrees).

Results and discussion.

Soft-NanoImprinting Lithography is performed following a simple procedure shown in Figure 1 and detailed in the Methods section. It involves mould degassing before application onto as-prepared xerogel in a relative humidity-controlled environment, consolidation at 120°C before unmoulding, and final curing at 450°C. The quality of the replica with respect to applied relative humidity, temperature and ageing time prior to imprinting was first fully investigated for TiO_2. It was then completed by similar, but more succinct,

investigations for Al_2O_3, hybrid and pure SiO_2, and Y-stabilized ZrO_2, to draw a more general picture of the study.

Soft-NIL imprinting of TiO_2 xerogel.

First, the relative mobility of TiO_2 xerogel with respect to the applied Relative Humidity (RH) during imprinting was assessed by measuring the height profile of final cured replica obtained with a mould bearing a single "large" square cavity with a height of 1 µm (Figure 2). The height was chosen to be largely superior to the xerogel thickness to ensure that the filling of the cavity is only partial. Due to the large lateral dimension of the cavity and the softness of the mould material, the latter tends to collapse at the centre when applied on the xerogel (Figure 2a). The outer edge of the cavity, presenting a step, is analysed by AFM and exhibits a specific profile (Figure 2b). A constant thickness of 100 nm is measured, by ellipsometry, at

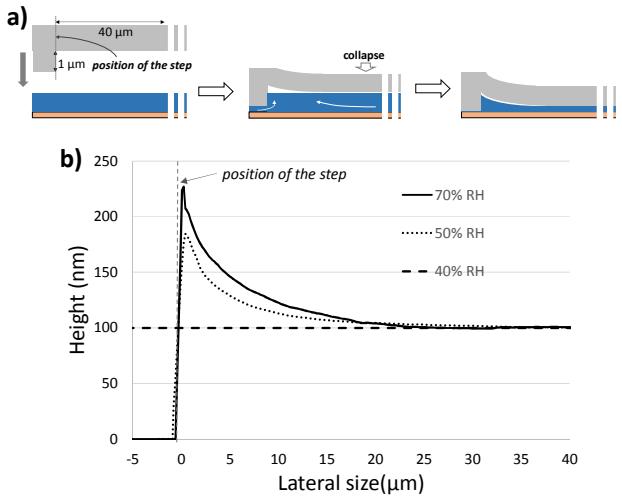

the theoretical step position at RH = 40%, suggesting that the imprinting did not occur at such humidity likely because of a too low xerogel mobility. On the other hand, for humidity above 40%, the mass transfer has clearly occurred as revealed by the presence of a thickness step formed at the cavity edge.

Figure 2: *a) Scheme of the mould deformation at the step edge during imprinting b) Replica thickness profiles, plotted from the step edge for 40, 50 and 70% RH.*

The thickness difference between each side of the step is around 200nm and roughly corresponds to the value expected if the mould surface on the left of the edge reaches the surface of the solid substrate (Figure 2b). As a result, most of the xerogel was displaced (from the left part to the right part) over a distance of at least 5 µm according to the assumption that it corresponds to the displaced volume on the right side of the step. On the right side, the height of the motif line is maximal at the edge and decreases gradually to reach the initial value of 100 nm at 20 µm from the edge. At 70% RH, a similar result is obtained with only a slightly higher motif at the edge. It suggests that above 40%RH, the fluidity of the xerogel is such that matter can be displaced from the edge of the cavity to over 20 µm. Note that the heights at the edge do not reach the maximal value of 1 µm imposed by the mould depth, which

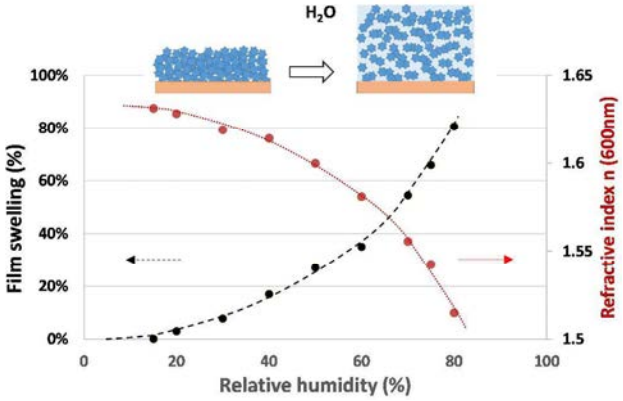

Figure 3*: Variation of thickness and refractive index of as-deposited TiO_2 xerogel films as a function of RH measured by environmental ellipsometry. Each point was measured independently (equilibrium took less than 1min). The dotted line is added as a guide for the eyes.*

can be expected from the insufficient initial volume of xerogel (100 nm thick xerogel layer in the present case).

These results confirm the crucial role of humidity on the xerogel mobility, and state that no imprinting can occur below a certain critical RH. It is difficult to establish exactly the strain field dispersion responsible for the material reorganisation. A simulation would be necessary but this is out of the scope of the present work. However, it is reasonable to expect that most of the mass is expelled from the surroundings of the cavity and accumulate at the edges of the cavity, displacing the xerogel to form the observed converging profile. In such conditions, where mass transport can extend over length scale of several microns, imprinting motifs of sub-micron sizes may only be limited by the xerogel fluidity.

At high RH, the absorption of water in the xerogel is promoted, which is expected to reduce its viscosity. This reduction will, in turn, lead to higher mobility. This can be quantified by directly measuring the evolution of a xerogel layer thickness – percentage of swelling/shrinkage - upon RH variation. Figure 3 displays such a swelling curve for an as-deposited TiO_2 xerogel film. The refractive index decreases with increasing relative humidity as water (n=1.33) is incorporated to the dry xerogel (n_{600nm}=1.63). The water uptake is not proportional to RH and tends to increase at higher humidity. This effect can be explained by the cumulative effect of the increasing xerogel hygroscopy with increasing water content and by a progressively weaker network offering less mechanical resistance to the absorption of water. At 40%RH, the xerogel is charged with around 8%$_{vol}$ of water and has been shown not flexible enough to be imprinted. At 50%RH, this uptake reaches 14% and allows imprinting. If RH is increased up to 80%, an uptake as high as 80% is observed. It is thus clear that a compromise is required. Indeed, on one hand, high RH must be used to allow efficient mass transfer while, on the other hand, low RH will reduce the potential shrinkage induced by the elimination of the absorbed water during annealing.

In the following experiment, morphology of TiO_2 replica, obtained at different relative humidity from 40% to 80%, from the same PDMS mould bearing micron-scale square arrays of square cavities (see Table 1 for exact dimensions) were investigated. The imprinting was performed 2 min after deposition in order to allow equilibration with the atmosphere without modifying too much the xerogel condensation degree. The time management is of particular importance and will be discussed in details later on in this article. The lateral dimension and height of the structures were measured both on the master and on the replica by AFM and SEM (Figure 4a) and Table 1) and were assumed to be identical between mould and master (negligible shrinkage applied during PDMS cross-linking). TiO_2 features exhibit the typical truncated square pyramids expected through imprinting from square cavities, as reported in previous studies.[16] No replication occurred below 50% relative humidity, while imprinting is efficient above 50% RH, confirming the results of Figure 2. Results are gathered in Figure 4b) together with the surface roughness of the replica deduced from AFM images. While, below 80% RH, replica show Root Mean Square Roughness (RMS) around 1 nm, those obtained at 80% RH present higher roughness (up to a factor of 4). Furthermore, AFM images of such replicas revealed numerous cracks and topographic inhomogeneities (see Figure 5).

The lateral dimension does not change significantly with the relative humidity after thermal treatment. Thus, the increase in the pyramid's height must mainly be due to the xerogel better infiltration into the mould cavities. Therefore, a relative humidity of 70%, which corresponds to 30%$_{vol}$ water content (Fig. 3), allows for an optimal filling of the mould cavities.

In this experiment, even if the shrinkage is expected to be higher at 80% RH than at 50% RH because of the increased amount of water present in the xerogel; it has not been evidenced experimentally. Importantly, the degassed PDMS mould pumps all volatile species, including water, from the xerogel. This pumping is critical since it first eliminates trapped air from the cavities, inducing efficient xerogel filling and second, it eliminates absorbed water from the xerogel at the PDMS interface, promoting even further filling. While the filling proceeds, the xerogel viscosity progressively increases - with the decrease of water content - up to the threshold from which the viscosity becomes too high to allow further mass transfer. Furthermore, the augmentation of viscosity is also a result of the polycondensation of the xerogel, which kinetic depends on the temperature. It is thus important to apply conditions (e.g. RH and temperature) allowing the slowest possible polycondensation to permit optimal filling as it will be demonstrated.

When the water content is too high (e.g. reaching more than 50% increase of the gel volume above 70%RH), the filling of the cavities is efficient but the pumping does not allow the full extraction of the absorbed water molecules from the xerogel. The xerogel stabilizes thus into a less dense state than at moderate humidity with water remaining trapped inside. Upon consolidation at 120°C, trapped water gather into microdomains driven by the inorganic network polycondensation before pervaporating eventually through the PDMS mould microporosity. [40] After unmoulding and during the final thermal annealing, the more fragile intermediate microporous TiO_2 network collapses on itself, revealing cracks, defects and high roughness. For such a reason, an optimal

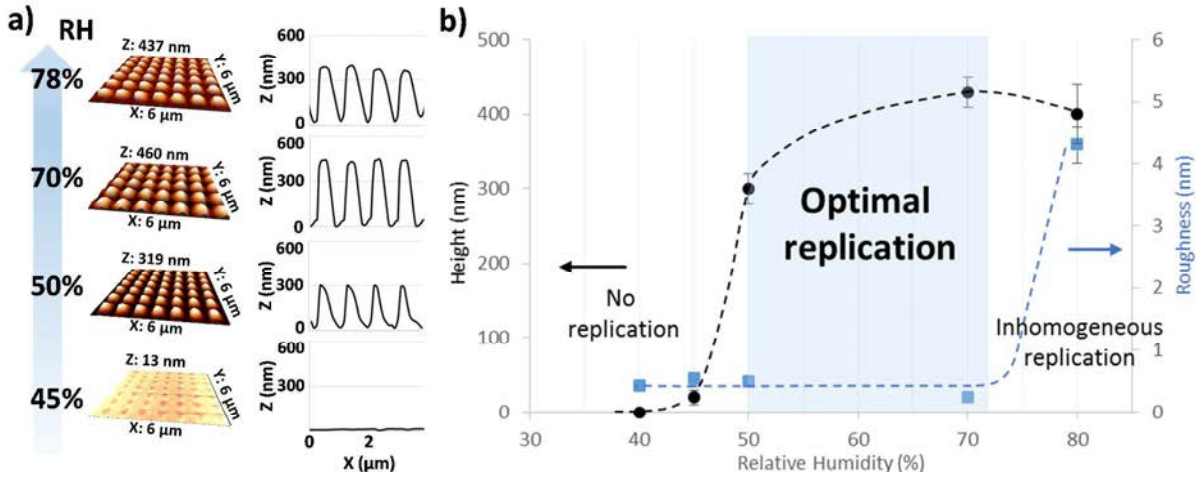

Figure 4: *a) AFM maps and profiles of the square arrays of square truncated pyramids with a 1 µm pitch imprinted at various relative humidity. b) Motif's height (circles) and roughness (squares) after thermal curing as a function of humidity.*

	Mould	Replica 45%	Replica 50%	Replica 70%	Replica 80%
Patterns height (nm)	**700 ± 20**	**20 ± 20**	**300 ± 20**	**430 ± 20**	**400 ± 40**
Lateral dimension (nm)	**700 ± 20**	**440 ± 20**	**440 ± 20**	**440 ± 20**	**460 ± 40**
RMS (nm)	**0.4**	**0.55**	**0.5**	**0.25**	**4.13**

Table 1: *Dimensions of the imprinted structures deduced from AFM and SEM.*

content in water exists - around 30% in volume – leading to patterns with the highest aspect ratios and homogeneity.

Figure 5 shows optical microscope Dark Field images of 20*20 μm^2 arrays, gathering each 400 square TiO_2 motifs imprinted at different humidity. Optical dark field imaging allows to collect the resonant scattered light from Mie modes formed within the pillars composing the arrays.[41] The spectral dispersion in the far field scattering is thus extremely sensitive to slight variations of motif size and shape. Similar visual appearance (colour and intensity) within each motif in dark field configuration accounts thus for its structural homogeneity. First, it is clear that arrays replicated at 80% RH exhibit bright additional scattering, especially outside the imprinted zones, associated to the formation of defects and cracks as mentioned above. At 45% RH, the scattering intensity of the motifs is very low compared to 50% RH and 70% RH as a result of its much lower motif height. It is clear that the 400 pillars present in each array feature negligible fluctuation of lateral dimensions and heights in the optimal range of humidity accounting for the low deviation determined by statistics on AFM (Table 1).

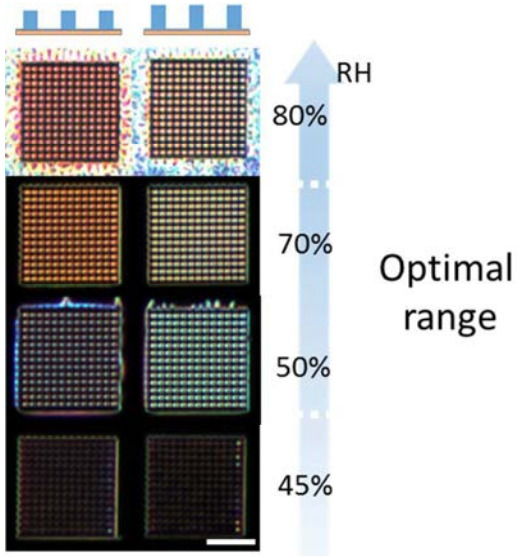

Figure 5: *Optical microscope dark field images of TiO_2 replicas imprinted at 45%, 50%, 70% and 80% RH, replicated from a mould bearing arrays of 400 pillars featuring 440 nm width, 1000 nm pitch and 700 nm depth (left array) or 1100 nm depth (right array). All the images are collected in the same conditions of illumination and detection to be directly compared. Color is homogeneous among the same array. Strong scattering around the structures due to cracks can be seen at 80% RH. Scale bar is 10 µm.*

Performing soft-NIL on sol-gel systems is thus very dependent on the relative humidity. Besides, it is known that as-prepared xerogel layers consolidate more or less rapidly through polycondensation with time and temperature. The xerogel may thus not be mobile enough to be imprinted after a certain time. In order to standardize soft-NIL processing on sol-gel resists, it is crucial to determine the imprintability time window for each metal oxide depending on the external temperature. First, one can use *in situ* environmental ellipsometry investigation on plain xerogel thin films to assess their transition from non-cohesive sol to cross-linked gels that dictates the imprintability of the material. This sol-gel transition, named gelation time, is a characteristic of any xerogel and varies only with the polycondensation kinetics. The measurement of this transition, first presented by Soler-Illia *et al* [37], is done by monitoring the variations of the refractive index and the swelling amplitude of an as-prepared xerogel with time, both directly related to the network condensation degree. This investigation necessitates a cycling between low (25% RH) and high (65% RH) humidity as presented in Figure 6. TiO_2 xerogel, and the other studied oxides, were cycled at different temperatures to measure their sol-gel transition and investigate the correlation between this transition and their ability to be easily imprinted. Figure 6a shows the variation of a TiO_2 xerogel refractive index (n) and thickness (t) at 30°C during humidity cycling. The global evolutions of t (decreasing with time) and n (increasing with time) suggest that the xerogel densifies as expected from the expulsion of water (syneresis) induced by the network progressive cross-linking and the progressive evaporation of HCl. [37]

During the first humidity cycles (from 0 to 70 min), the

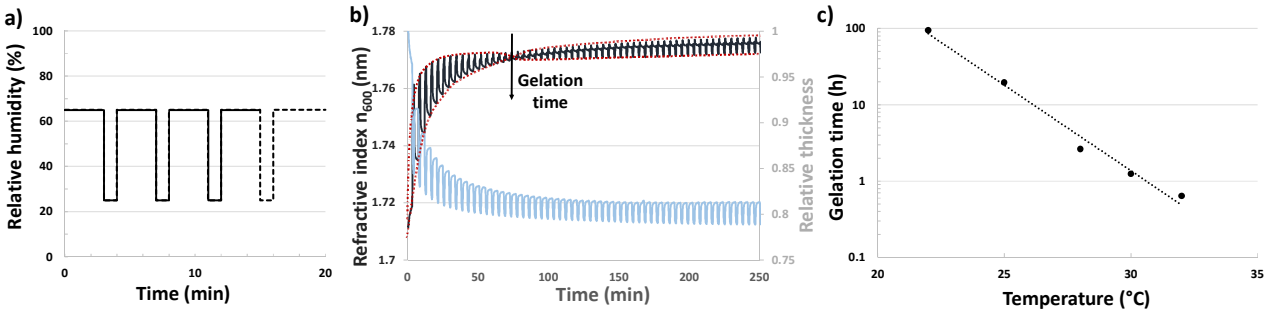

Figure 6: *a) Determination of TiO_2 xerogel gelation time corresponding to the inversion of the refractive index dependence to RH (top curve) at 30°C. The relative thickness shrinkage (bottom curve) with respect to RH cycling and ageing time is presented on the same graphic. Inset: humidity ramp cycled in the ellipsometry chamber during the measurement. b) Extracted gelation time for TiO_2 xerogel as a function of temperature in semi-log scale. The dotted line represents an*

refractive index of the film decreases while the thickness increases at high humidity, and inversely at low humidity, indicating a swelling of the xerogel by water absorption (the refractive index of water is lower than that of the xerogel at any time). For both variables, the amplitude between high and low RH diminishes progressively, due to the xerogel progressive stiffening. At 70 min, a critical point (the gelation time) is reached where an inversion of the amplitude is observed only for the refractive index. The only possible explanation for such an inversion of the refractive index amplitude involves a complete change of the network behaviour over water successive up-take and departure. After the gelling time, the network is stiffened enough so that it does not completely collapse, and micro-cavities of air are formed, upon water desorption. Because air has a lower refractive index than water, the global measured refractive index of the porous xerogel is thus now inversed, being lower at low humidity than at high humidity where water adsorbs and condenses replacing the air from the pores. In summary, the gelling time (or point) corresponds to the xerogel state where the 3D framework can withstand the presence of empty micro-pores. In less stiff 3D frameworks, such as those present before 70 min, micro-pores tend to collapse, due to the strong Laplace pressure applying at their highly curved interface, which leads to the thickness decrease. The gelling point observed by this method is thus a good indication of the relative kinetics of xerogel layer condensation.

The determination of the gelation time vs temperature has been also investigated using the same experimental protocol but by modifying the temperature of the sample during the experiment using a Peltier modulus (experimental data not shown). The corresponding plot of the gelation time vs temperature in Figure 6b) gives a good indication of the condensation kinetic dependence to the temperature for the present TiO_2 xerogel layer system. The gelation time is shown to decrease quasi-exponentially with respect to the temperature ($t_{gel} = A.e^{-\alpha T}$ where α=0.52°C^{-1}) with a fairly good correlation (R^2=0.995), confirming that the imprintability window of TiO_2 xerogel must be much shorter at high temperature.

The critical effect of time and temperature on the imprintability of sol-gel was verified on the same TiO_2 xerogel, using the same custom-designed chamber as described before and using a PDMS mould patterned with a diffraction grating composed of lines (dimensions: 190 ± 30 nm wide; 180 nm height; grating pitch 1 µm). Optical images of the diffraction grating replica are shown in Fig. 7a). Keeping RH and T constant at 50% and 22°C, respectively, the diffraction intensity is better after 5' than after 6'30", to eventually disappear totally after 8', confirming the critical role of aging time. It is important to note that only the intensity is compared as the colour of the diffracted light is dependent on the measurement angle. The topography of the replicated gratings was evaluated using AFM as shown in Figure 7a). The

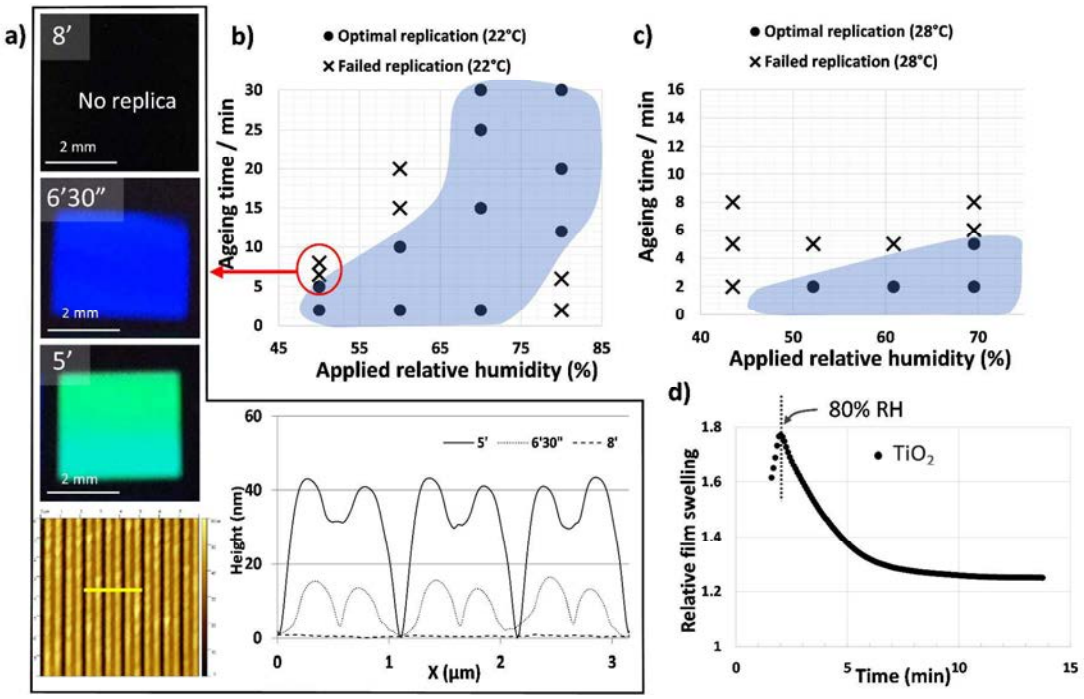

Figure 7: *a) Optical images and AFM profiles showing the diffraction of the TiO_2 replicas imprinted at 22°C and 50% RH after 5, 6.5 and 8 minutes (respectively first, second and third panel from the top). AFM map of the diffraction grating imprinted after 5 minutes is shown in the bottom panel. Mould motifs are parallel lines (190 ± 30 nm wide, 180 nm height, 1 µm pitch). b), c) Imprintability diagrams obtained at 22°C and 28°C, respectively ("good" and "poor" replicas are represented by round points and crosses, respectively). d) Evolution of as-prepared TiO_2 xerogel swelling with time when exposed to RH = 80% (reference initial thickness is taken at RH < 10%).*

dual peak deformation visible on the AFM profiles, is likely due to the visco-elastic properties of the xerogel and its interaction with the cavities during filling as explained elsewhere with polymeric resins.[42] Investigated imprinting conditions were: ageing times from 2 to 30 min, temperatures fixed at 22°C or 28°C, and RH between 50% and 80%. Efficiencies of replication are summarized in diagrams Figures 7b) and 7c) for 22°C and 28°C respectively. "Good quality" replica feature 40 nm tall lines and intense diffraction are represented by round points while "poor quality" replica show less than 20 nm tall lines and non-homogeneous or defects are represented by crosses.

At 50% RH, good replicas are prepared up to 5 min of ageing, while this period increases to 12 min and above 30 min for 60% and 70% RH, respectively. This shift originates from the lower condensation rate of the network when water is present in high quantity in the xerogel. The optimal viscoelastic property of the xerogel is thus maintained for longer periods at such intermediate humidity. In addition, the cross-linking is accompanied by water expulsion from the network which also participates to the mobility adjustment as revealed in Figure 7d). Indeed, just after deposition, applying 80% RH to the film induces the maximal 80% swelling after 3 min as already shown in Figure 3. Then, the film starts to shrink back, as a result of the network condensation, to reach around 25% residual swelling after 10min. Therefore, the optimal mobility of the as-prepared TiO_2 xerogel can also be achieved at high humidity but for longer periods of ageing. This decrease of the water content in the gel with aging, even at high humidity, explains why the gel maintained at 80%RH must be aged at least 15 min before yielding good replicas. This property is extremely important since it gives more time for potential intermediate operations before imprinting (*e.g.* system transfer, mould aligning, atmosphere adjustment…), which is a real issue in sol-gel processing.

To go further, we investigated the possibility to prepare replicas when the temperature is increased up to 28°C during ageing. Diagram c) of Figure 7 gathers the conditions leading to "good" and "poor" replicas (RH values correspond here to $100*P/P_0$, with P_0 the saturated vapour pressure at 28°C). As water uptake decreases and inorganic condensation rate increases with temperature, the conditions for which optimal conditions are present exists at much lower ageing times, as expected. Only high humidity allow to extend the imprintability time over 5 min. This emphasizes again the real dependence of sol-gel systems to external conditions for nano-imprinting, as already demonstrated for dip-coating [38] but certainly also for other processes. Besides, not all sol-gel systems evolve with the same kinetics and TiO_2 xerogels from $TiCl_4$ sols are known to have a relatively slow condensation, which is ideal for nano-imprinting.

TiO_2 skrinkage.

As mentioned, soft-NIL process of transition metal oxides and in particular TiO_2, is accompanied by a more or less significant degree of shrinkage. In the present study, shrinkage was measured for 2D (plain film) by ellipsometry and for 1D (lines) and 0D (square motifs) by AFM. These investigations are gathered in Figure 8. First transversal shrinkage of the plain 2D film, was assumed to be equivalent to the total volume shrinkage. It was measured by ellipsometry to be 50% between as-prepared (2 min/10% RH) and 120°C, and 70% after treatment at 450°C (see Figure 8a). Measuring the dimensions of the imprinted motifs before pre-treatment at 120°C, underneath the mould is impossible. Thus it is assumed that 1D and 0D motifs already shrank of $50\%_{vol}$ at 120°C, as for the plain xerogel layer. By taking this into account, the overall shrinkage (from as-prepared to 450°C) for 1D and 0D motifs can be extrapolated from the measurements at 120°C and 450°C. For 1D structures (lines motifs studied above), the shrinkage is greater for the height (43%) than for the width (25%). This can be explained by the fact that, on the one hand, vertical shrinkage induces less stress for the overall structure due to the substrate-structure interaction, and on another hand, shrinkage in the shorter dimension of the object is facilitated. For 0D structures (studied previously), it is interesting to note that shrinkage is greater horizontally (37%) than vertically (27%) even if the inverse trend was expected in view of the previous observations for lines. This effect is yet not fully understood. Further systematic investigations are on the way to better assess and predict the anisotropic shrinkage depending on the morphology and orientation of the motifs with respect to the surface. In the present conditions, where chloride salt precursors are used and controlled humidity is applied, the volume shrinkage is 20% lower than previous reports[26] and inherent to the precursor chemistry. In particular, the height shrinkage is twofold lower than in previous studies (only 27% against more than 56%

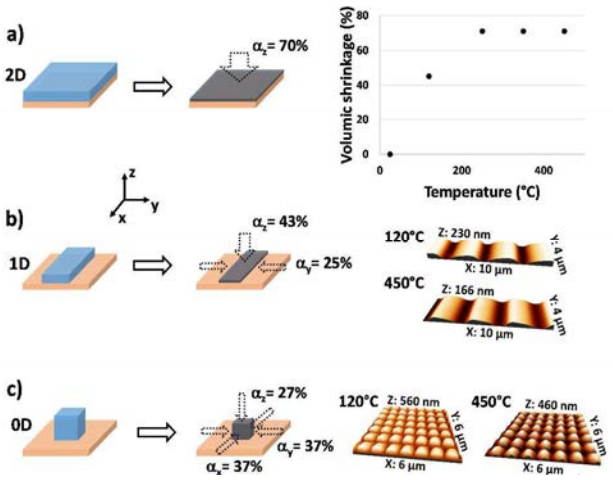

Figure 8: *Schematic representation of shrinkage in a) 2D, plain layer structure with the evolution of the thickness during annealing between 25°C and 450°C obtained from in situ ellipsometry; b) a 1D, line structure and c) a 0D, point structure. AFM 3D maps of studied structures after annealing at 120°C for 10 mins and after 450°C for 10 mins are also provided for lines and point structures.*

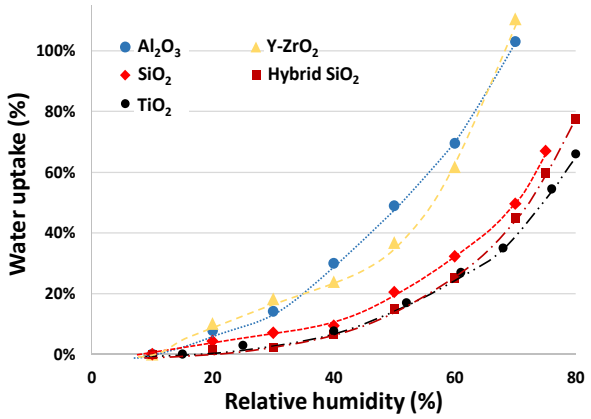

Figure 9: *Water uptake of various as-prepared xerogels with respect to relative humidity measured by in situ time-resolved ellipsometry. Dashed lines are displayed as guides*

previously[26]) making it particularly interesting for high Z ratio structures. Refractive index was measured to be $n(\lambda) = 2.05 + 0.05/\lambda^2$ for TiO_2 after annealing at 450°C.

Soft-NIL imprinting of (hybrid-) SiO_2, Al_2O_3, and Y-ZrO_2 xerogels compared to TiO_2.

Three other xerogel systems were selected and compared to TiO_2. These materials are among the most used sol-gel materials and are known to present different affinity to water and different rates of condensation under xerogel form. The swelling-dependence to humidity plots for as-prepared xerogel layers are shown in Figure 9. They reveal that all the investigated materials have the ability to uptake water and swell in the ideal range of about 30%. While silica-based and TiO_2 systems exhibit similar behaviours, Y-ZrO_2 and Al_2O_3 are much more hygroscopic since they can swell up to 110% of their initial thickness at 70%RH. The corresponding gelation time, obtained experimentally following the same procedure used for TiO_2 xerogels (data not shown) are given in Table 2. Al_2O_3 and Y-ZrO_2 have gelation times that extend over several hours, like TiO_2, while silica-based systems stiffen much faster with gelation times inferior to 30 min. This can be explained by the slow condensation rate of non-silica systems due to the high acidity associated with the use of chloride precursors. Silica-based systems are also in high acidic medium that is known to catalyse condensation, resulting in faster gelation. Indeed, pure silica xerogel (from TEOS precursor) could not be imprinted even just after deposition and whatever the humidity and temperature, despite its ability to swell. It reveals that as-prepared silica xerogels rapidly crosslinks into a rigid network. In the case of hybrid (methylated) silica xerogel obtained with $40\%_{mol}$ MTEOS and $60\%_{mol}$ TEOS, the condensation rate decreases as less hydroxyl groups are

Table 2: *Results of gelation time measurements at 25°C for the various studied xerogels.*

Material	TiO_2	SiO_2	Hybrid-SiO_2	Al_2O_3	Y-ZrO_2
Gelation time (h) at 25°C	**19.7**	**0.26**	**0.53**	**11.5**	**> 80**

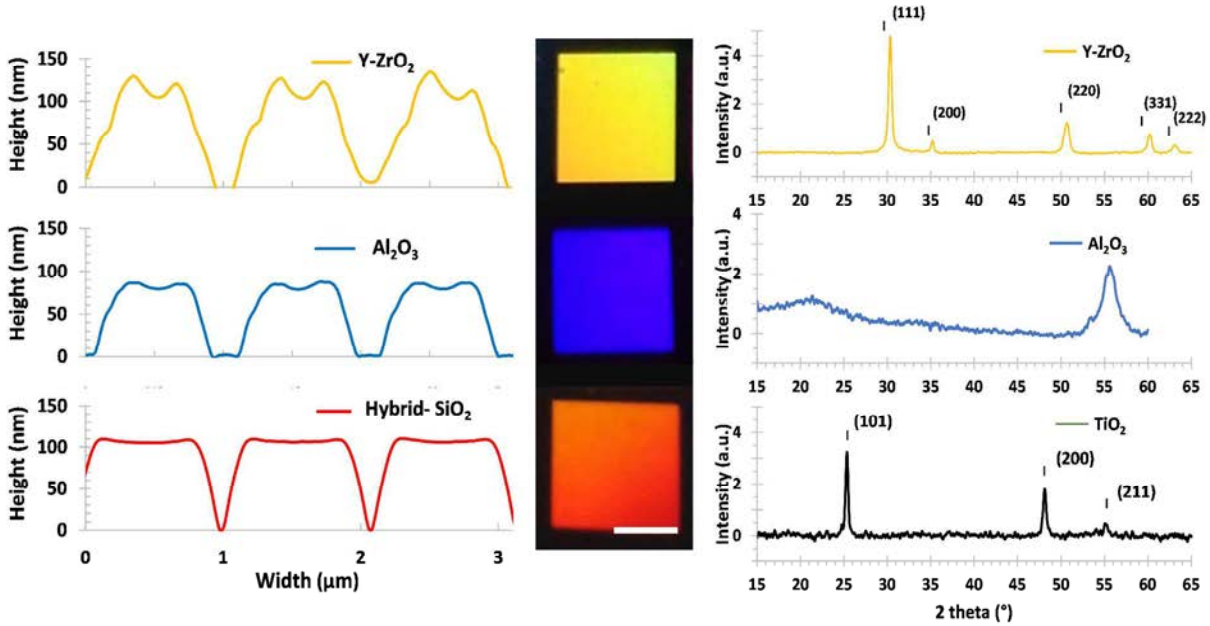

Figure 10: *Characterizations of Y-ZrO_2 (top), Al_2O_3 (middle) and hybrid-SiO_2 (bottom) diffraction gratings (same grating parameters than Figure 7) imprinted in optimal conditions. From the left to the right panel: AFM profiles, optical images of the diffraction (scale is 2mm) and X-ray diffraction patterns for each material (Y-ZrO_2 and TiO_2 were acquired in Bragg-Brentano geometry and respectively indexed with PDF #00-030-1468 and PDF #00-021-1272, Al_2O_3 acquisition was performed in GIXRD configuration).*

present for cross-linking. Gelation time measurements show that condensation is around
two-fold slower than that fond for pure SiO_2. An imprintability window of up to 4 min after deposition was determined at 70% RH and 22°C.

Diffraction grating replicas were then produced from a mould patterned with light diffraction gratings composed of lines with the following dimensions: 190 ± 30 nm wide; 180 nm height; grating pitch 1 µm. Optimal imprinting conditions, deduced from the gelation time and water uptake for each system, were applied. These conditions correspond to water uptake of 35% (RH = 50%; T = 25°C; t = 2 mins) for Y-ZrO_2, of 25% (RH=35%; T = 28°C; t = 1 mins) for Al_2O_3, and of 35% (RH = 70%; T = 22°C; t < 1 min) for hybrid-SiO_2.
AFM height profiles are provided in Figure 10, together with the corresponding optical and XRD characterisations. AFM and optical images confirms that the imprinting is homogeneous over 5 x 5 mm for Y-ZrO_2, Al_2O_3 and hybrid-SiO_2 and that good quality replicas can be obtained with different metal oxides when the conditions are adjusted such that water uptake in the as-prepared xerogel remains close to 30% in volume. The differences in AFM profile shape and relative gap between lines is due to the relative shrinkage of the materials. Y-ZrO_2 shows a rougher surface caused by the growth of larger crystallites during the annealing step.
In XRD measurements, a shift of the diffraction peaks towards lower diffraction angle is seen for Y-ZrO_2 probably due to a slight deviation in composition compared to the reference pattern (PDF #00-030-1468). In the case of Al_2O_3, replica were further heated at 1000°C for 2 h (8°C/min). However, even in GIXRD geometry, no diffraction peak can be detected for the expected α-Al_2O_3 phase: the measured pattern exhibits only a peak centered at 56° corresponding to the Si substrate (311) Bragg reflection (in Bragg diffraction conditions for such GIXRD geometry) and a broad signal around 20° probably due to amorphous SiO_2 contribution. The absence of α-Al_2O_3 diffraction lines may be due to the presence of too small nano-crystallized domains providing a too small diffraction volume to be detected with a conventional X-ray source. TiO_2 replicas show the typical diffraction peaks of Anatase phase.

Conclusions.

In summary, we demonstrated that soft-NIL can be applied to many conventional sol-gel systems and can lead to high quality, reproducible and homogeneous replicas with a minimal shrinkage. In particular, optimal replicas are obtained by a careful selection of precursors and chemical conditions, but also by accurately controlling the temperature, humidity and xerogel layer ageing time before and during imprinting. In particular, we demonstrated that the optimal conditions correspond to a water uptake equivalent to 30%$_{vol}$ of the xerogel film during imprinting, for all studied sol-gel systems.

Acknowledgement.

The authors acknowledge the funding by A*MIDEX (reference. ANR- 11-IDEX-0001-02) and MATISSE, the facilities of the NANOTECMAT platform at the IM2NP and of the CP2M of Aix-Marseille University.

References.

(1) Garín, M.; Fenollosa, R.; Alcubilla, R.; Shi, L.; Marsal, L. F.; Meseguer, F. All-Silicon Spherical-Mie-Resonator Photodiode with Spectral Response in the Infrared Region. *Nat. Commun.* **2014**, *5*, 3440.

(2) Evlyukhin, A. B.; Novikov, S. M.; Zywietz, U.; Eriksen, R. L.; Reinhardt, C.; Bozhevolnyi, S. I.; Chichkov, B. N. Demonstration of Magnetic Dipole Resonances of Dielectric Nanospheres in the Visible Region. *Nano Lett.* **2012**, *12* (7), 3749–3755.

(3) Person, S.; Jain, M.; Lapin, Z.; Saenz, J. J.; Wicks, G.; Novotny, L. Demonstration of Zero Optical Backscattering from Single Nanoparticles. *Nano Lett.* **2013**, *13* (4), 1806–1809.

(4) Chong, K. E.; Hopkins, B.; Staude, I.; Miroshnichenko, A. E.; Dominguez, J.; Decker, M.; Neshev, D. N.; Brener, I.; Kivshar, Y. S. Observation of Fano Resonances in All-Dielectric Nanoparticle Oligomers. *Small* **2014**, *10* (10), 1985–1990.

(5) Miroshnichenko, A. E.; Evlyukhin, A. B.; Yu, Y. F.; Bakker, R. M.; Chipouline, A.; Kuznetsov, A. I.; Luk'yanchuk, B.; Chichkov, B. N.; Kivshar, Y. S. Nonradiating Anapole Modes in Dielectric Nanoparticles. *Nat. Commun.* **2015**, *6*, 8069.

(6) Proust, J.; Bedu, F.; Chenot, S.; Soumahoro, I.; Ozerov, I.; Gallas, B.; Abdeddaim, R.; Bonod, N. Chemical Alkaline Etching of Silicon Mie Particles. *Adv. Opt. Mater.* **2015**, *3* (9), 1280–1286.

(7) Spinelli, P.; Verschuuren, M. a; Polman, a. Broadband Omnidirectional Antireflection Coating Based on Subwavelength Surface Mie Resonators. *Nat. Commun.* **2012**, *3*, 692.

(8) Kim, K. S.; Jeong, H.; Jeong, M. S.; Jung, G. Y. Polymer-Templated Hydrothermal Growth of Vertically Aligned Single-Crystal ZnO Nanorods and Morphological Transformations Using Structural Polarity. *Adv. Funct. Mater.* **2010**, *20* (18), 3055–3063.

(9) Moitra, P.; Slovick, B. A.; Li, W.; Kravchencko, I. I.; Briggs, D. P.; Krishnamurthy, S.; Valentine, J. Large-Scale All-Dielectric Metamaterial Perfect Reflectors. *ACS Photonics* **2015**, *2* (6), 692–698.

(10) Moitra, P.; Slovick, B. A.; Gang Yu, Z.; Krishnamurthy, S.; Valentine, J. Experimental Demonstration of a Broadband All-Dielectric Metamaterial Perfect Reflector. *Appl. Phys. Lett.* **2014**, *104* (17), 171102.

(11) Abbarchi, M.; Naffouti, M.; Vial, B.; Benkouider, A.; Lermusiaux, L.; Favre, L.; Ronda, A.; Bidault, S.; Berbezier, I.; Bonod, N. Wafer Scale Formation of Monocrystalline Silicon-Based Mie Resonators via Silicon-on-Insulator Dewetting. *ACS Nano* **2014**, *8* (11), 11181–11190.

(12) Naffouti, M.; David, T.; Benkouider, A.; Favre, L.; Ronda, A.; Berbezier, I.; Bidault, S.; Bonod, N.; Abbarchi, M.

Fabrication of Poly-Crystalline Si-Based Mie Resonators via Amorphous Si on SiO2 Dewetting. *Nanoscale* **2016**, *8* (5), 2844–2849.
(13) http://www.rolith.com http://www.rolith.com.
(14) Biswas, A.; Bayer, I. S.; Biris, A. S.; Wang, T.; Dervishi, E.; Faupel, F. Advances in Top-down and Bottom-up Surface Nanofabrication: Techniques, Applications & Future Prospects. *Adv. Colloid Interface Sci.* **2012**, *170* (1–2), 2–27.
(15) Dalstein, O.; Ceratti, D. R.; Boissière, C.; Grosso, D.; Cattoni, A.; Faustini, M. Nanoimprinted, Submicrometric, MOF-Based 2D Photonic Structures: Toward Easy Selective Vapors Sensing by a Smartphone Camera. *Adv. Funct. Mater.* **2016**, *26*, 81–90.
(16) Bottein, T.; Wood, T.; David, T.; Claude, J. B.; Favre, L.; Berbézier, I.; Ronda, A.; Abbarchi, M.; Grosso, D. "Black" Titania Coatings Composed of Sol-Gel Imprinted Mie Resonators Arrays. *Adv. Funct. Mater.* **2016**, *27* (2).
(17) Sanchez, C.; Boissiere, C.; Grosso, D.; Laberty, C.; Nicole, L. Design, Synthesis, and Properties of Inorganic and Hybrid Thin Films Having Periodically Organized Nanoporosity. *Chem. Mater.* **2008**, *20* (3), 682–737.
(18) C. J. Brinker; G. W. Scherer. *Sol–Gel Science: The Physics and Chemistry of Sol–Gel Processing*; Elsevier, 1990.
(19) Peroz, C.; Heitz, C.; Barthel, E.; Søndergård, E.; Goletto, V. Glass Nanostructures Fabricated by Soft Thermal Nanoimprint. *J. Vac. Sci. Technol. B Microelectron. Nanom. Struct.* **2007**, *25* (4), L27.
(20) Peroz, C.; Chauveau, V.; Barthel, E.; Søndergård, E. Nanoimprint Lithography on Silica Sol-Gels: A Simple Route to Sequential Patterning. *Adv. Mater.* **2009**, *21* (5), 555–558.
(21) Letailleur, A.; Teisseire, J.; Chemin, N.; Barthel, E.; Søndergård, E. Chemorheology of Sol-Gel Silica for the Patterning of High Aspect Ratio Structures by Nanoimprint. *Chem. Mater.* **2010**, *22* (10), 3143–3151.
(22) Yang, K. Y.; Yoon, K. M.; Choi, K. W.; Lee, H. The Direct Nano-Patterning of ZnO Using Nanoimprint Lithography with ZnO-Sol and Thermal Annealing. *Microelectron. Eng.* **2009**, *86* (11), 2228–2231.
(23) Brigo, L.; Mattei, G.; Michieli, N.; Brusatin, G. 2D Photonic Gratings from Thermal Imprinting of ITO-Based Films. *Microelectron. Eng.* **2012**, *97*, 193–196.
(24) Yu, C. C.; Chen, H. L. Nanoimprint Technology for Patterning Functional Materials and Its Applications. *Microelectron. Eng.* **2015**, *132*, 98–119.
(25) Kim, W.-S.; Yoon, K. B.; Bae, B.-S. Nanopatterning of Photonic Crystals with a Photocurable Silica–titania Organic–inorganic Hybrid Material by a UV-Based Nanoimprint Technique. *J. Mater. Chem.* **2005**, *15* (42), 4535.
(26) Richmond, D. a.; Zhang, Q.; Cao, G.; Weiss, D. N. Pressureless Nanoimprinting of Anatase TiO2 Precursor Films. *J. Vac. Sci. Technol. B Microelectron. Nanom. Struct.* **2011**, *29* (2), 21603.
(27) Park, H. H.; Choi, D. G.; Zhang, X.; Jeon, S.; Park, S. J.; Lee, S. W.; Kim, S.; Kim, K. D.; Choi, J. H.; Lee, J.; Yun, D. K.; Lee, K. J.; Park, H. H.; Hill, R. H.; Jeong, J. H. Photo-Induced Hybrid Nanopatterning of Titanium Dioxide via Direct Imprint Lithography. *J. Mater. Chem.* **2010**, *20* (10), 1921–1926.
(28) Hlaing, H.; Lu, X.; Nam, C. Y.; Ocko, B. M. Water-Vapor-Assisted Nanoimprinting of PEDOT:PSS Thin Films. *Small* **2012**, *8* (22), 3443–3447.
(29) Kothari, R.; Beaulieu, M. R.; Hendricks, N. R.; Li, S.; Watkins, J. J. Direct Patterning of Robust One-Dimensional, Two-Dimensional, and Three-Dimensional Crystalline Metal Oxide Nanostructures Using Imprint Lithography and Nanoparticle Dispersion Inks. *Chem. Mater.* **2017**, *29* (9), 3908–3918.
(30) Spinelli, P.; Macco, B.; Verschuuren, M. A.; Kessels, W. M. M.; Polman, A. Al2O3/TiO2 Nano-Pattern Antireflection Coating with Ultralow Surface Recombination. *Appl. Phys. Lett.* **2013**, *102* (23), 2011–2015.
(31) Khorasaninejad, M.; Chen, W. T.; Devlin, R. C.; Oh, J.; Zhu, A. Y.; Capasso, F. Metalenses at Visible Wavelengths: Diffraction-Limited Focusing and Subwavelength Resolution Imaging. *Science* **2016**, *352* (6290), 1190–1194.
(32) Gutruf, P.; Zou, C.; Withayachumnankul, W.; Bhaskaran, M.; Sriram, S.; Fumeaux, C. Mechanically Tunable Dielectric Resonator Metasurfaces at Visible Frequencies. *ACS Nano* **2016**, *10*, 133–141.
(33) Zou, C.; Gutruf, P.; Withayachumnankul, W.; Zou, L.; Bhaskaran, M.; Sriram, S.; Fumeaux, C. Nanoscale TiO2 Dielectric Resonator Absorbers. *Opt. Lett.* **2016**, *41* (15), 3391.
(34) Crepaldi, E. L.; De, G. J.; Soler-Illia, A. A.; Grosso, D.; Cagnol, F.; Ribot, F. O.; Ment Sanchez, C. Controlled Formation of Highly Organized Mesoporous Titania Thin Films: From Mesostructured Hybrids to Mesoporous Nanoanatase TiO 2. *J. Am. Chem. Soc.* **2003**, *125*, 9770–9786.
(35) Grosso, D.; Faustini, M.; Dalstein, O.; Bottein, T.; Cattoni, A. Nanoimprint Lithography Process and Patterned Substrate Obtainable Therefrom. EP17305286.1, 2017.
(36) Cattoni, A.; Cambril, E.; Decanini, D.; Faini, G.; Haghiri-Gosnet, A. M. Soft UV-NIL at 20 Nm Scale Using Flexible Bi-Layer Stamp Casted on HSQ Master Mold. *Microelectron. Eng.* **2010**, *87* (5–8), 1015–1018.
(37) Soler-Illia, G. J. a. a.; Angelomé, P. C.; Fuertes, M. C.; Grosso, D.; Boissiere, C. Critical Aspects in the Production of Periodically Ordered Mesoporous Titania Thin Films. *Nanoscale* **2012**, *4* (8), 2549.
(38) Grosso, D.; Cagnol, F.; Soler-Illia, G. J. D. A. A.; Crepaldi, E. L.; Amenitsch, H.; Brunet-Bruneau, A.; Bourgeois, A.; Sanchez, C. Fundamentals of Mesostructuring through Evaporation-Induced Self-Assembly. *Adv. Funct. Mater.* **2004**, *14* (4), 309–322.
(39) Folch, A.; Schmidt, M. A. Wafer-Level in-Registry Microstamping. *J. Microelectromechanical Syst.* **1999**, *8* (1), 85–89.
(40) Barrie, J. a.; Machin, D. The Sorption and Diffusion of Water in Silicone Rubbers: Part I. Unfilled Rubbers. *J. Macromol. Sci. Part B* **1969**, *3* (4), 645–672.
(41) Sun, S.; Zhou, Z.; Zhang, C.; Gao, Y.; Duan, Z.; Xiao, S.; Song, Q. All-Dielectric Full-Color Printing with TiO2 Metasurfaces. *ACS Nano* **2017**, *11* (5), 4445–4452.

(42) Rowland, H. D.; Sun, A. C.; Schunk, P. R.; King, W. P. Impact of Polymer Film Thickness and Cavity Size on Polymer Flow during Embossing: Toward Process Design Rules for Nanoimprint Lithography. *J. Micromechanics Microengineering* **2005**, *15* (12), 2414–2425.